Monthly Notices
of the
ROYAL ASTRONOMICAL SOCIETY

MNRAS **494,** 5923–5935 (2020)
Advance Access publication 2020 May 1

doi:10.1093/mnras/staa826

Non-thermal models for infrared flares from Sgr A*

Eric Petersen[1]★ and Charles Gammie[1,2]

[1]*Physics, University of Illinois at Urbana-Champaign, 1110 W. Green St., Urbana, IL 61801, USA*
[2]*Astronomy, University of Illinois at Urbana-Champaign, 1002 W. Green St., Urbana, IL 61801, USA*

Accepted 2020 March 18. Received 2020 March 18; in original form 2019 May 22

ABSTRACT

Recent observations with mm very long baseline interferometry (mm-VLBI) and near-infrared (NIR) interferometry provide mm images and NIR centroid proper motion for Sgr A*. Of particular interest are the NIR flares that have more than an order of magnitude higher flux density than the quiescent state. Here, we model the flares using time-dependent, axisymmetric, general relativistic magnetohydrodynamic (GRMHD) simulations with an electron distribution function that includes a small, variable, non-thermal component motivated by magnetic reconnection models. The models simultaneously match the observed mm mean flux density, mm image size, NIR quiescent flux density, NIR flare flux density, and NIR spectral slope. They also provide a better fit to the observed NIR flux density probability density function than previously reported models by reproducing the power-law tail at high flux density, though with some discrepancy at low flux density. Further, our modelled NIR image centroid shows very little movement: centroid excursions of more than 10 μas (the resolution of GRAVITY) are rare and uncorrelated with flux.

Key words: accretion, accretion discs – black hole physics – MHD.

1 INTRODUCTION

It is well established (e.g. Ghez et al. 2008; Gillessen et al. 2009; Genzel, Eisenhauer & Gillessen 2010) that there is a supermassive black hole at the centre of the Milky Way Galaxy. This region of the sky has been observed in the radio, mm, near-infrared (NIR), and X-ray bands. It contains a radio source, Sgr A*(e.g. Balick & Brown 1974; Falcke et al. 1998; Baganoff et al. 2001; Genzel et al. 2003). Existing models (e.g. Falcke et al. 2011; Shiokawa et al. 2012) have been able to match observations of the mm light curve, and modeling of the mm polarization is ongoing (e.g. Dexter 2016; Liu et al. 2016; Mościbrodzka & Gammie 2018). Event Horizon Telescope (EHT) has already provided mm-wavelength images that resolve the black hole in M87 (Event Horizon Telescope Collaboration 2019a, b, c, d, e, f) and will soon provide mm-wavelength images of Sgr A* that resolve the scale of the accretion flow and that can be compared to images produced by various fluid models (see Noble et al. 2007; Mościbrodzka et al. 2009; Ricarte & Dexter 2015). The NIR light curve, which shows more variability than the mm light curve (e.g. Ghez et al. 2005; Witzel et al. 2018), has not been modelled as successfully. Sgr A* also flares in the X-ray (see e.g. Baganoff et al. 2001; Ponti et al. 2015), but the focus of this work is on infrared variability.

For Sgr A*, the mean 1.3-mm (230 GHz) flux density is 3.7 Jy (Bower et al. 2015), with a standard deviation of ∼0.7 Jy; see also Fish et al. (2011); Haubois et al. (2012); Bower, Plambeck & Marrone (2013); and Liu et al. (2016). The 1.3-mm source is resolved with a full width at half maximum (FWHM) of 37 μas (see Doeleman et al. 2008).

During 2.2 μm (1.4 THz) flares, observations by Witzel et al. (2012) show that $\nu L_\nu \propto \nu^\alpha$ with $\alpha \approx 0.4$ (see also Gillessen et al. 2006; Hornstein et al. 2007; Marrone et al. 2008; and Dodds-Eden et al. 2009). Do et al. (2009) report variability that is not periodic or quasi-periodic. Dodds-Eden et al. (2011) claim that, above 5 mJy, the 2.2-μm flux distribution function follows a power law with index 2.7. Observations at 4.5 μm reported in Hora et al. (2014) show a continuous ∼24-h light curve with the flux density usually below 5 mJy and the flare lasting for a few hours.

In this work, we take the distance to Sgr A* to be $(7.85 \pm 0.14 \pm 0.04)$ kpc and the mass of the central black hole to be $M_{\rm BH} = (4.02 \pm 0.16 \pm 0.04) \times 10^6\,{\rm M}_\odot$ (see Boehle et al. 2016). However, after our calculations were finished, new estimates of $(8.178 \pm 0.013 \pm 0.022)$ kpc for the distance and $M_{\rm BH} = (4.152 \pm 0.014) \times 10^6\,{\rm M}_\odot$ for the mass have been released by Abuter et al. (2019). Measurements of the linear polarization led Bower et al. (2005) to place an upper bound of $10^{-7}\,{\rm M}_\odot\,{\rm yr}^{-1}$ on the accretion rate of Sgr A*. Marrone et al. (2006) find $2 \times 10^{-9}\,{\rm M}_\odot\,{\rm yr}^{-1} < \dot{M} < 2 \times 10^{-7}\,{\rm M}_\odot\,{\rm yr}^{-1}$ based on rotation measure and a model for $n_{\rm e}(r)$ and $B(r)$. In terms of the Eddington accretion rate ($\dot{M}_{\rm Edd} \equiv \frac{4\pi G M_{\rm BH} m_p}{\epsilon c \sigma_T}$ with the radiative efficiency, ϵ, set to 0.1) these bounds are $2 \times 10^{-8}\dot{M}_{\rm Edd} < \dot{M}_{\rm SgrA*} < 2 \times 10^{-6}\dot{M}_{\rm Edd}$.

The GRAVITY collaboration has released Very Large Telescope Interferometer observations of Sgr A*in the NIR band (Gravity

★ E-mail: eapeter2@illinois.edu

Collaboration 2018). While this instrument does not resolve the disc (Eisenhauer et al. 2008), it is able to measure the centroid of the emission with an accuracy of ∼10 μas. This allows a small, brightly emitting region near the event horizon to be tracked for multiple dynamical times during a flare. There are thus two probes of the region close to the black hole that motivate models of the accretion flow.

The NIR and mm emission in Sgr A* are predominately generated by the synchrotron process (Yuan & Narayan 2014). The synchrotron emissivity depends on the electron distribution function.

Dissipation in collisionless astrophysical plasmas is a subject of much interest (e.g. Loureiro & Boldyrev 2017; Chasapis et al. 2018; Gary et al. 2018; Qin, Kong & Zhang 2018) because it affects source observational appearance through synchrotron emission and Compton scattering. There are three distinct routes through which dissipation can occur. The first is through an Alfvénic cascade (Howes 2010; Kawazura, Barnes & Schekochihin 2018; Verniero, Howes & Klein 2018), which differentially heats the ions and electrons in a manner dependent on plasma β (the ratio of gas pressure to magnetic pressure). The second route to dissipation is through shocks. This depends on the Mach number of the turbulence that is driven in part by the magnetic field. The fraction of energy going to electrons and the resulting electron spectrum downstream from collisionless shocks is an area of continuing research (e.g. Guo, Sironi & Narayan 2018; van Marle, Casse & Marcowith 2018). Finally, dissipation can occur in current sheets. This is the route that will be examined throughout this work.

Some researchers have attempted to explain the NIR flares using thermal models (e.g. Dexter & Fragile 2013; Chan et al. 2015). Because it is difficult for a single thermal distribution function to produce the correct mm flux and produce large enough NIR flux to explain the observed flares, these models rely on NIR emission from small, heated regions being gravitationally lensed. Other work (e.g. Özel, Psaltis & Narayan 2000; Chan et al. 2009; Dodds-Eden et al. 2010) has used non-thermal electron models but has not produced flares as large as observed. A satisfactory flare was produced by Ball et al. (2016) using a β-dependent non-thermal electron injection scheme, but the resulting NIR spectral slope did not match observations.

Here, we describe an attempt to develop a model motivated by particle-in-cell (PIC) simulations that accelerates, at a rate proportional to J^2, electrons in reconnecting current sheets into a κ distribution function (see e.g. Pierrard & Lazar 2010, for a review of κ distribution function). Synchrotron cooling then causes the non-thermal electrons to relax toward a thermal distribution as they are advected through the disc. This model is expected to rapidly change non-thermal populations and create flares at frequencies above what would be expected from a thermal model alone. These flares also provide seed photons for Compton scattering that have the potential to produce an X-ray flare; this will be discussed in future work. Our model is deployed in the context of axisymmetric general relativistic magnetohydrodynamic (GRMHD) models; three-dimensional (3D) models will also be considered in future work.

The plan of this paper is as follows: Section 2 discusses prior flaring models, the distribution functions used in this work, PIC simulations that motivate the models used here, and four models for injecting and cooling electrons to and from the non-thermal distribution function; Section 3 reviews the observations, the numerical schemes used, and the parameters chosen to fit the observations; in Section 4, results are presented for mm wavelengths (including light curves and images), NIR wavelengths (including light curves, flux histograms, and image centroid wander), and spectral energy distributions (SEDs); Section 5 provides a discussion of the results of this model as they compare both to observations and previous models as well as a brief description of future work; and finally, Section 6 provides a summary.

2 NON-THERMAL ELECTRON MODELS

2.1 Non-thermal acceleration and cooling

Magnetohydrodynamics (MHD) turbulence naturally leads to the development of current sheets. Some current sheets are dynamic and caused by propagating Alfvénic discontinuities, perhaps formed by steepening of Alfvén waves in a compressible plasma (see Cohen & Kulsrud 1974). Others are nearly stationary and may transition to a turbulent state, perhaps due to the plasmoid instability (see Loureiro, Schekochihin & Cowley 2007).

We further hypothesize that the effect of the turbulent-resistive dissipation is to remove particles from the thermal (Maxwell–Jüttner) distribution that describes the bulk of the electrons and place them in a non-thermal distribution. We model the non-thermal component using a κ distribution function:

$$\frac{\mathrm{d}n_{\mathrm{e,NT}}}{\mathrm{d}\gamma \mathrm{d}cos\xi \mathrm{d}\phi} = n_{\mathrm{e,NT}} \frac{N}{4\pi} \gamma \left(\gamma^2 - 1\right)^{1/2} \left(1 + \frac{\gamma - 1}{\kappa w}\right)^{-(\kappa+1)}. \quad (1)$$

Here, $n_{\mathrm{e,\,NT}}$ is the number density of electrons in the non-thermal component, N is a normalization constant that depends on κ and w, and the momentum space coordinates are γ, ξ, and ϕ (Lorentz factor, pitch angle, and gyrophase, respectively). The κ distribution has three parameters: κ, w, and $n_{\mathrm{e,\,NT}}$.

The κ distribution has a thermal component at low γ and then smoothly transitions to a power law at high γ, with no low-γ power-law cutoffs that would be unstable to a bump-on-tail-like instability. The κ distribution was initially studied as a fit to weakly collisional plasma in the Earth's magnetosphere (Vasyliunas 1968; Pierrard & Lazar 2010).

Siversky & Zharkova (2009) show a two-dimensional (2D) PIC simulation of an ion–electron plasma (with the proton-to-electron mass ratio set to 100), with a wide electron distribution function (with its width similar to its mean) arising in a current sheet. Riquelme et al. (2012) report 2D PIC simulations, with mass ratios from 1 to 20, that show electron heating due to both viscosity and reconnection. Heating in the reconnection region produced a power-law tail with $\mathrm{d}n/\mathrm{d}\gamma \sim \gamma^{-1.5}$.

A local shearing-box model of a collisionless disc is presented by Kunz, Stone & Quataert (2016). They solved a hybrid model with a full kinetic treatment of the ions and an isothermal fluid model for the electrons. These models contain no information about the electron distribution function, but it is interesting to note that the ion distribution function is well fit by a κ distribution with $\kappa \approx 5$.

Further information about accelerated electron distribution functions can be found in Biskamp (1996); Liu et al. (2011); Cerutti et al. (2012); Cerutti et al. (2013); Cerutti et al. (2014); Sironi & Spitkovsky (2014); and Makwana et al. (2017).

In what follows, we consider a combined thermal–non-thermal distribution function. The total electron number density $n_{\mathrm{e}} = n_{\mathrm{e},\,T} + n_{\mathrm{e,\,NT}}$, where $n_{\mathrm{e,\,NT}}$ is the number density of electrons in the non-thermal component. The thermal component has a dimensionless temperature $\Theta_{\mathrm{e}} \equiv kT_{\mathrm{e}}/(m_{\mathrm{e}}c^2)$. We set $w = \Theta_{\mathrm{e}}$. Fig. 1 shows the combined distribution function for a typical set of distribution function parameters.

The observed NIR spectral slope of Sgr A* constrains the slope of the distribution function and therefore κ. NIR photons are produced

by electrons in the power-law tail of the κ distribution where $\mathrm{d}n/\mathrm{d}\gamma \propto \gamma^{-p}$ and $p = \kappa - 1$. The emissivity $j_\nu \propto \nu^{-(p-1)/2}$. Thus, if the source is optically thin $\nu L_\nu \propto \nu j_\nu \propto \nu^{(2-\kappa/2)}$ so for a source with $\nu L_\nu \sim \nu^\alpha$,

$$\kappa = 4 - 2\alpha. \tag{2}$$

In Sgr A*, $\alpha = 0.4$ at NIR frequencies; thus, we set $\kappa = 3.2$.

Analytic fits to the unpolarized emission and absorption coefficients (j_ν and κ_ν, respectively) for the κ distribution are given in Pandya et al. (2016), equations 35–42.

2.2 Models for evolution of non-thermal electron population

In this paper, we will consider four models for the evolution of the non-thermal electron population, which here means the number density of non-thermal electrons, $n_{\mathrm{e,NT}}$.

Model A is purely thermal and serves to tie this work to previous work.

Model B places a constant fraction of electrons into a κ distribution; this can be compared to previous work with a constant fraction of electron energy in a power-law distribution.

Model C accounts for reconnection by setting $n_{\mathrm{e,\,NT}} \propto J^2$, where J is the magnitude of the three-current density measured in the frame of the plasma. This model is useful because it is less computationally expensive than the more realistic model D, below, but may none the less produce similar NIR light curves and has a similar physical motivation.

Model D accelerates electrons into the κ distribution with a rate density that is proportional to J^2. It then allows the non-thermal electrons to be advected with the flow. Finally, it permits them to cool, a process that we model here by returning electrons to the thermal part of the distribution function. Model C is the limit of model D with the cooling time set to zero. In Appendix B, we consider the effects of varying the cooling time and κ.

In model D the non-thermal electron population evolves according to

$$\frac{\mathrm{d}n_{\mathrm{e,NT}}}{\mathrm{d}\tau} = \eta\,\Omega(r)\left(n_{\mathrm{e,tot}} - n_{\mathrm{e,NT}}\right)\frac{J^2}{J_0^2} - \frac{n_{\mathrm{e,NT}}}{\tau_{\mathrm{cool}}}. \tag{3}$$

Here, $\mathrm{d}/\mathrm{d}\tau$ is a Lagrangian derivative, i.e. the rate of change in the plasma frame, $n_{\mathrm{e,\,NT}}$ is the number density of non-thermal electrons, $n_{\mathrm{e},\,T}$ is the number density of thermal electrons, $\Omega(r) = (GM/r^3)^{1/2}$ is the local Keplerian orbital frequency (without relativistic corrections), J^2 is the square of the local 3-current density, η is a dimensionless parameter that controls the efficiency with which currents accelerate electrons into the non-thermal distribution function, and J_0 is a characteristic 3-current density.

The characteristic current density J_0 is determined as follows. In a non-relativistic setting, $\vec{J} = c\vec{\nabla} \times \vec{B}/(4\pi)$, so $J^2 \sim c^2B^2/(16\pi^2L^2)$, where L is a characteristic length scale which we set to r. We assume that the magnetic pressure $B^2/8\pi$ is of order the gas pressure P. With these substitutions, and dropping factors of order unity, $J_0^2 \equiv \frac{c^2P}{r^2}$.

The synchrotron cooling time depends, in general, on the Lorentz factor γ and magnetic field strength B:

$$t_{\mathrm{cool,s}} = \frac{9}{4}\frac{m_{\mathrm{e}}^3c^5}{e^4}\frac{1}{\gamma B^2} \tag{4}$$

(e.g. Padmanabhan 2000). It is not possible to consistently incorporate this into our model because we adopt a single, constant form for the electron distribution function. Instead, we adopt a highly simplified model in which cooling is modelled by shifting electrons from the non-thermal component to the thermal component of the distribution function on a time-scale τ_{cool}. We can estimate τ_{cool} from the cooling time for NIR-producing electrons in a field B that is typical for models of Sgr A*. Using $B \simeq 30$G and taking ν appropriate to 2.2 μm photons, we find $\tau_{\mathrm{cool}} \approx 200\,\mathrm{s} \approx 10\,GM_{\mathrm{BH}}/c^3$ for $M_{\mathrm{BH}} = 4 \times 10^6\,\mathrm{M}_\odot$.

In the absence of cooling and acceleration, the non-thermal electrons are assumed to be advected with the flow and, therefore, obey a continuity equation $(n_{\mathrm{e,\,NT}}u^\mu)_{;\,\mu} = 0$, where u^μ is the plasma four-velocity.

2.3 Convergence of J^2

In models C and D, the evolution of the non-thermal electron density depends on the current density J. In what follows, we will determine J from ideal GRMHD simulations (e.g. Gammie, McKinney & Tóth 2003) where dissipation is not explicitly modelled. Instead, dissipation is modelled *implicitly* through the numerical scheme, in what is sometimes known as an Implicit Large Eddy Simulation (ILES, see e.g. Miesch et al. 2015). The current density will, therefore, be sensitive to numerical resolution. Does it make sense to use a numerical evaluation of J in the electron acceleration model?

Suppose that the dissipation were modelled explicitly using a scalar resistivity. Using a simple model of resistive dissipation in a relativistic plasma, it is possible to show that the fluid-frame heating rate per unit volume is J^2/σ, where σ is the conductivity and J is the 3-current density in the fluid frame. This is shown in Appendix A. The total dissipation rate is then $\int d^3x(J^2/\sigma)$. This total dissipation rate must be approximately independent of σ if the evolution of the turbulent energy is controlled by the largest scale structures in the turbulence, as would be the case for purely hydrodynamic turbulence at large Reynolds number.

Although our ILES models do not model dissipation explicitly, we expect that dissipation will occur close to the grid scale, Δx. The effective numerical resistivity is thus $\propto \Delta x$, and the effective conductivity is $\propto 1/\Delta x$. If this model is correct, then the total dissipation rate is $\propto (\Delta x)^{-1}\int d^3xJ^2$. This will converge in our ILES model even if J does not.

To test this idea, we consider a model 2D MHD turbulence problem, the Orszag-Tang vortex, over a large range in resolution. Fig. 2 shows J^2 for a non-relativistic Orszag–Tang vortex at a resolution of 128^2, 1024^2, and 8192^2. Evidently, the current structure changes as the resolution increases. The current sheets break up into islands and sub-islands, perhaps due to the plasmoid instability as in Loureiro et al. (2007).

Fig. 3 shows the evolution of $(\Delta x)^{-1}\int d^3xJ^2$ in a superset of the models shown in Fig. 2. Evidently, the evolution of the total dissipation rate *does* converge at high enough resolution. We conclude that it is possible to use $\int J^2$ to model the dissipation rate in a convergent fashion.

3 SOURCE MODEL

In our model, the flow of plasma around the black hole is described by a 2D GRMHD model. We will consider 3D models in a later publication. The GRMHD model is evolved together with equation (3), which provides a density of thermal and non-thermal electrons at every point in space time. We then produce synthetic observations using ray tracing at 1.3 mm and at 2.2 μm and fix the model parameters so as to match the mean observed 1.3-mm and 2.2-μm flux densities.

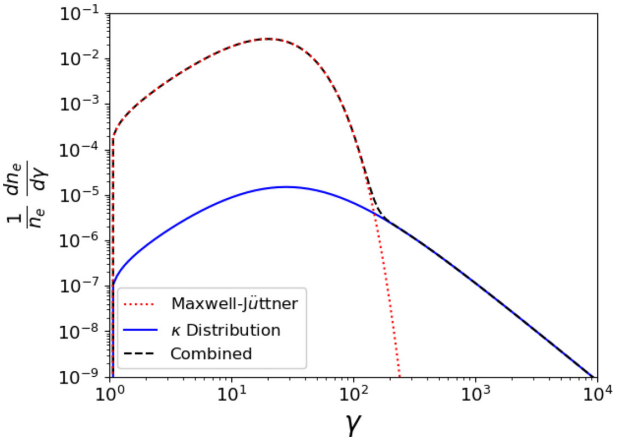

Figure 1. The distribution function model consists of a thermal distribution at low γ that transitions smoothly to the power-law tail. This figure shows an example in which $\Theta_e = w = 10$, $\kappa = 3.2$, and the non-thermal fraction, by number density, for the combined distribution function is 0.2 per cent.

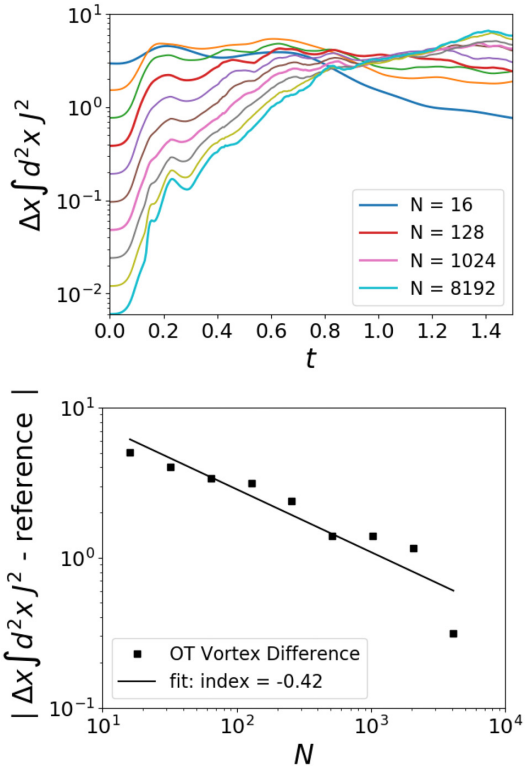

Figure 2. *Top:* Evolution of $\frac{1}{N} J^2$ (resistive heating) for various resolutions of an Orszag–Tang vortex test. *Bottom:* Convergence of $\frac{1}{N}\langle J^2 \rangle$ for the same resolutions, relative to the highest resolution (8192 × 8192).

3.1 GRMHD: `harm`

The basis for the accretion model in this work is the conservative, axisymmetric GRMHD code `harm`,[1] outlined in Gammie et al. (2003) and McKinney & Gammie (2004). The initial state is a Fishbone–Moncrief torus (Fishbone & Moncrief 1976) seeded with a magnetic field that follows isodensity contours in the

[1]Source code available at https://github.com/AFD-Illinois/iharm2d

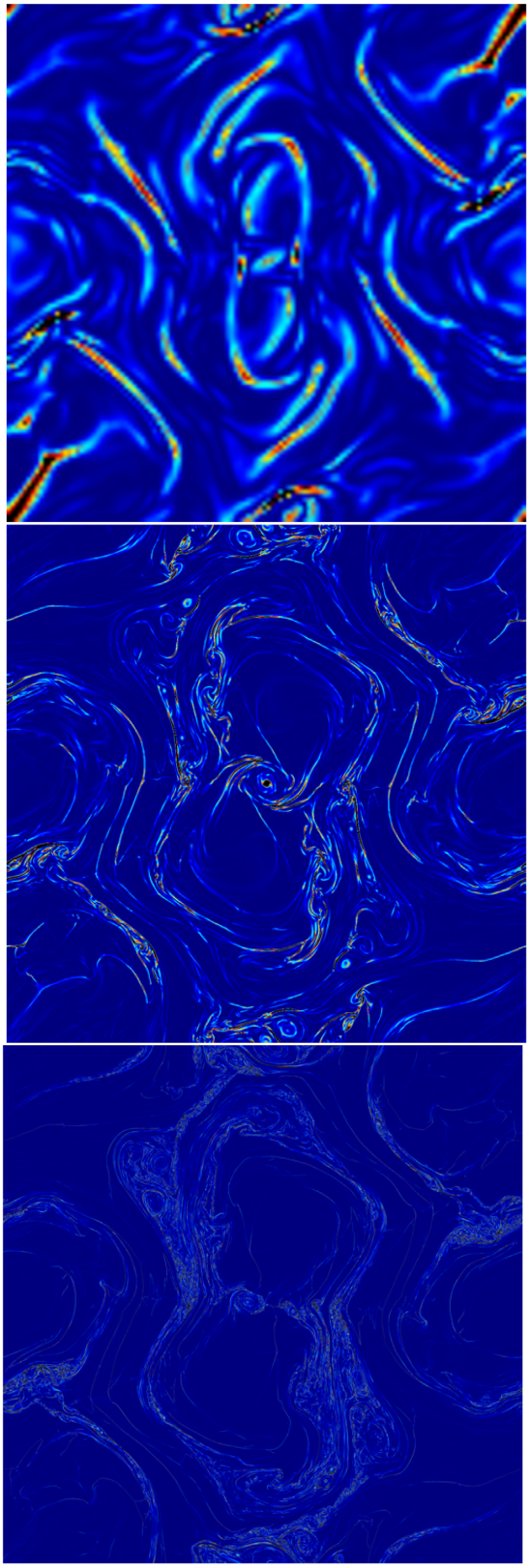

Figure 3. Snapshot of the squared current density in non-relativistic evolutions of the Orszag–Tang vortex using a version of the `harm` code at three resolutions and a common time. *Top:* 128^2; *centre:* 1024^2; and *bottom:* 8192^2. As resolution increases, the current sheets break up into turbulent substructures.

poloidal plane. This test is evolved in the Kerr metric for 3000 $GM_{\rm BH}/c^3$(∼16.5 h).

`harm` updates a list of primitive variables (rest mass density, ρ, internal energy, u, three components of the fluid three-velocity, v^i, and ${}^*F^{it}$, where F^{it} is the Faraday tensor). At the beginning of each time-step, the primitive variables (collectively called P) are converted to conserved variable U:

$$U = \sqrt{-g}\left(\rho u^t, T^t_t, T^t_i, B^i\right). \quad (5)$$

Here $g \equiv \det\left(g_{\mu\nu}\right)$ and T^μ_ν is the stress-energy tensor defined in Misner, Thorne & Wheeler (1973). Then, U is evolved and converted back to P. The forward operation $U(P)$ is analytic, but the inverse $P(U)$ is not.

A secant method is used to find $P(U)$ using the primitives from the prior time-step as the initial guess. We use parabolic reconstruction to calculate primitive values at zone faces from primitive values at zone centres. These values are then used to analytically calculate the left and right local Lax–Friedrichs fluxes, $F_{\rm L}$ and $F_{\rm R}$, as well as an approximate fast magnetosonic speed in both directions, $c_{\pm,\,\rm L}$ and $c_{\pm,\,\rm R}$. The maximum wave speed is defined by taking $c_{\rm top} \equiv \max\left(0, |c_{-,\,\rm L}|, |c_{-,\,\rm R}|, |c_{+,\,\rm L}|, |c_{+,\,\rm R}|\right)$. The no-monopoles constraint, $\vec{\nabla}\cdot\vec{B} = 0$, is maintained to machine precision per time-step using flux-interpolated constrained transport (Tóth 2000).

In our model, a ninth primitive variable, the number density of non-thermal electrons $n_{\rm e,\,NT}$, is also evolved. The non-thermal electrons are advected in the same manner as ρ. For model D, the value of $n_{\rm e,\,NT}$ is updated as described in Section 2.2 at each time-step. The evolution of the rest of the fluid is unaffected by $n_{\rm e,\,NT}$. In this work, all simulations use a `harm` resolution of 256 x 256 in the radius and the latitude.

3.2 Ray tracing: `ibothros`

Once we have a model for the velocity, magnetic field, and thermal and non-thermal electron densities from `harm`, we need to produce synthetic images. This is done using the `ibothros` ray-tracing code (Noble et al. 2007).

`ibothros` solves the geodesic equation backward along rays from individual pixels in a 'camera' that observes the source from a particular inclination:

$$\frac{{\rm d}x^\mu}{{\rm d}\lambda} = k^\mu \quad (6)$$

$$\frac{{\rm d}k_\mu}{{\rm d}\lambda} = -\Gamma^\alpha_{\mu\beta}k_\alpha k^\beta, \quad (7)$$

where λ is an affine parameter, $\Gamma^\alpha_{\mu\beta}$ is a connection coefficient, and k^μ is a tangent vector along the geodesic. `ibothros` also solves the covariant radiative transfer equation in the form

$$\frac{\rm d}{{\rm d}\lambda}\left(\frac{I_\nu}{\nu^3}\right) = \left(\frac{j_\nu}{\nu^2}\right) - (\kappa_\nu\nu)\left(\frac{I_\nu}{\nu^3}\right). \quad (8)$$

Here, ν is the frequency of the radiation in the plasma frame, ${\rm d}\lambda$ is the affine parameter, and j_ν, κ_ν, and I_ν are the plasma-frame emissivity, absorptivity, and intensity, respectively. I_ν/ν^3, j_ν/ν^2, and $\nu\kappa_\nu$ are invariant.

The step size ($\Delta\lambda$) is set adaptively, with the constraint that the largest step size is smaller than the `harm` grid size to ensure adequate sampling of the fluid. Smaller step sizes are used in regions where the intensity changes rapidly. At every step, a bilinear interpolation of the `harm` variables is used to calculate the local emissivity and absorptivity. Depending on the model (see Section 2.2), j_ν and κ_ν are either thermal or a weighted average of thermal and κ emissivities (see Pandya et al. 2016). In this work, we compute light curves by integrating over 256^2 pixel synthetic images that have a 35 $GM/(c^2D)$ field of view.

3.3 Parameter determination

The GRMHD and ray-tracing parameters can affect the characteristics of the simulated flux. Table 1 summarizes what these parameters are called, what they mean, and which observations are used to constrain them. Table 2 lists our chosen values for each model. The spin of the black hole, a, is simply set to 15/16, in line with previous work (see Mościbrodzka et al. 2009), and is chosen so as not to overproduce X-ray emission. Similarly, the correct mm image size is maintained by setting the ion–electron temperature ratio ($T_{\rm p}/T_{\rm e}$) and the angle between the observer and the black hole spin (the inclination angle, i) to values from Mościbrodzka et al. (2009).

Finally, the 2.2-μm flux is matched to the largest NIR flux during a flare by controlling the fraction of electrons in the non-thermal distribution. This is accomplished differently for each of the four models described in Section 2.2. In model A, there is no parameter and the NIR flux cannot be adjusted. Model B has a uniform (in time and space) fraction of the electrons, ${\rm NT_{frac}} \equiv n_{\rm e,\,NT}/n_{\rm e,\,tot}$, in the κ-distribution. In model C, $n_{\rm e,NT} = C\, n_{\rm e,tot}\, J^2/J_0^2$. Model D has two adjustable parameters. The first is the injection efficiency, η; the NIR flux increases as η is increased. The second is $\tau_{\rm cool}$; increasing $\tau_{\rm cool}$ increases the NIR flux. Increasing the cooling parameter also has the effect of smearing out peaks in the NIR light curve caused by sudden bursts of non-thermal electron injection. The effects of changes to κ and $\tau_{\rm cool}$ are explored in Appendix B.

4 RESULTS

For each model, we calculate synthetic images, light curves, and SEDs. Existing mm observations can be adequately modelled without invoking any non-thermal component, so they serve as a constraint on the model. The models match the observed NIR spectral slope and flare amplitude. Table 2 summarizes the results for each model.

4.1 230-GHz results

The simulated outputs of the models of Section 2.2 can be compared to the observational constraints listed in Section 1. Fig. 4 compares the flux to the observed mean flux of 3.7 Jy (Bower et al. 2015). All models have mean mm flux densities within 15 per cent (0.7σ) of 3.7 Jy. Both the observed mm light curves and the model light curves show substantial variability ($\sigma \approx 0.7$ Jy).

Fig. 5 shows a representative image of the inner 35 $GM_{\rm BH}/c^2$ (∼1.6 AU or ∼200 μas) taken from model D at time 1000 $GM_{\rm BH}/c^3$ (∼5.5 h). The elliptical Gaussian fit is given by the solid white ellipse while the observed size, quoted as 37 μas in Section 1 and originally reported by Doeleman et al. (2008) is traced by the dashed green circle. The size (measured by solid angle) ratio of the fit to the observations is 1.00; the fit size fluctuates by about 15 per cent, so it is somewhat unusual to match the observed size this well. The average sizes for all models are between 35 μas and 37 μas. For all models, the mass of the simulated disc ($\mathcal{M}$) needed to satisfy these mm constraints implies an accretion rate of $\dot{M} \approx 2.3 \times 10^{-9}\,{\rm M_\odot\,yr^{-1}} \approx 2.6 \times 10^{-8}\dot{\rm M}_{\rm Edd}$.

Table 1. Summary of the model parameters and the observations (Section 1) that constrain them.

Symbol	Description	Observational constraint
a	Black hole spin	X-ray emission (see Mościbrodzka et al. 2009)
T_p/T_e	Ion-electron temperature ratio	Mean mm flux
$\mathcal{M}$	Mass of disc	Mean mm flux/image size
i	Viewing angle	mm image size
κ	NT distribution parameter	NIR spectral index
η	NT injection efficiency	Mean NIR flux
$\tau_{\rm cool}$	Non-thermal e^- cooling time	Mean NIR flux
C	Constant in $n_{\rm e,NT} = Cn_{\rm e,tot}J^2/J_0^2$	Mean NIR flux
$\rm NT_{frac}$	Constant ratio $n_{\rm e,\ NT}/n_{\rm e,\ tot}$	Mean NIR flux

Table 2. Summary of the parameters and output for the models A–D. See Section 2.2 for an explanation of each model, Section 3.3 and table Section 1 for information on the model parameters, and Section 4 for a description of the results.

	Model A	Model B	Model C	Model D
a	15/16	15/16	15/16	15/16
T_p/T_e	3.0	3.0	3.0	3.0
$\mathcal{M}(10^{19}$ grams)	2.0	2.0	2.0	2.0
i (degrees)	83.8	83.8	83.8	83.8
κ	N/A	3.2	3.2	3.2
$\rm NT_{frac}$	N/A	2.0×10^{-3}	N/A	N/A
C	N/A	N/A	3.0×10^{-3}	N/A
η	N/A	N/A	N/A	$1/3 \times 10^{-6}$
$\tau_{\rm cool}$ (seconds)	N/A	N/A	N/A	200
$\dot{M}$ (10^{-9} $M_\odot$ $\rm yr^{-1}$)	2.3	2.3	2.3	2.3
Mean mm flux (Jy)	3.2	3.2	3.2	3.2
s.d. of mm flux (Jy)	0.72	0.74	0.72	0.74
mm image size (μas)	35	36	35	36
Quiescent NIR flux (mJy)	0.010	15	0.69	0.12
Flaring NIR flux (mJy)	4.5	40	22	25
NIR centre max dev. (μas)	16.1	2.13	4.29	22.0
NIR centre rms dev. (μas)	3.8	1.0	1.3	2.4
NIR centre dev. >10 μas	3.7%	0.0%	0.0%	0.3%
Flaring spectral slope	− 1.6	0.32	0.37	0.38
Quiescent spectral slope	− 2.3	0.41	0.42	0.38

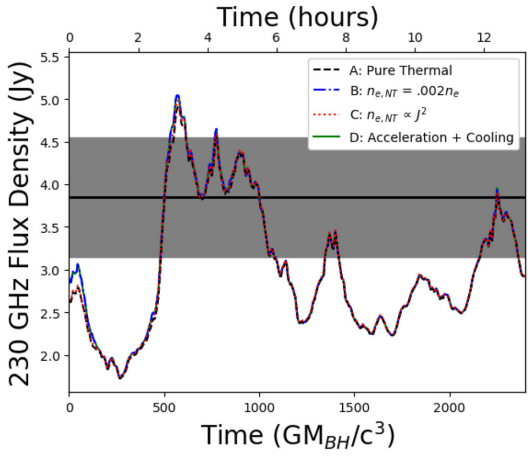

Figure 4. Light curves for models A–D at 1.3 mm. The light curves match almost exactly, indicating that changes in the non-thermal population have little impact on the 230- GHz flux in our models. The observed mean mm flux density (3.7 Jy, compared to 3.2 Jy in models A–D) is given by the solid black line and the grey region shows the observed 1σ variability (0.7 Jy, compared to 0.7 Jy in the models).

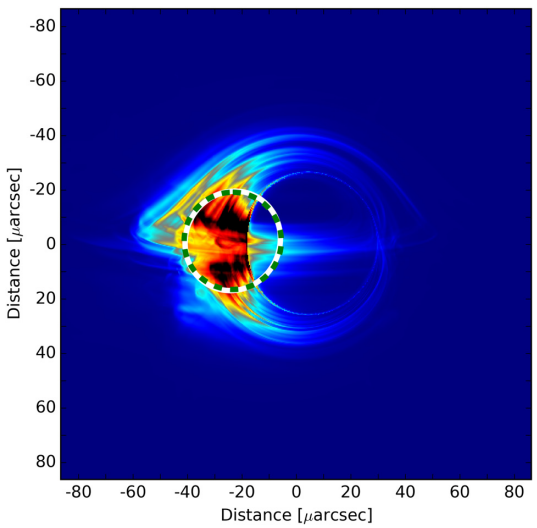

Figure 5. A simulated 230- GHz image from model D at $t = 1000\ GM_{\rm BH}/c^3$ ($\sim$ 5.5 h). The colour scale is linear and shows brighter regions as black or red and dimmer regions as dark or light blue. The solid white ellipse shows a 2D Gaussian fit to the image and the dashed green circle shows the observed image size (see Section 1).

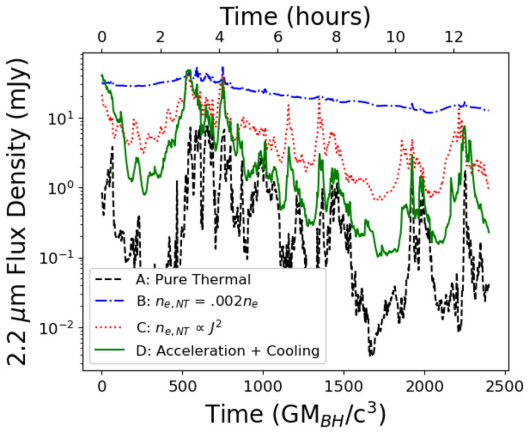

Figure 6. 2.2-μm light curves for models A–D. The thermal model (dashed black line) does not produce enough total flux or variability to match observations. The constant non-thermal fraction model (dashed– dotted blue line; model B) can be made to match the total flux but not the variability. The injection models, both with instantaneous cooling (dotted red line; C) and with finite cooling (solid green line; D), do show substantial variability. The flares can be made to match or exceed the observed flare amplitude.

4.2 2.2- μm results

Fig. 6 shows NIR light curves for models A–D. Compared to the observations, the thermal model (model A) vastly underproduces NIR flux density, with average over 50 $GM_{\rm BH}/c^3 \approx 4.5$ mJy and little variance. The non-thermal models produce maximum flux densities that are closer to observations (40 mJy, 22 mJy, and 25 mJy for models B, C, and D, respectively). These models do not all create the observed variability (see Fig. 7 for the flux distribution), however. Model B can be tuned to produce either an approximately correct flux in the flaring state (as shown in Fig. 6) or the correct quiescent flux but never produces both with the same parameters. Model B's mean quiescent flux, averaged from 1675 $GM_{\rm BH}/c^3$ to 1725 $GM_{\rm BH}/c^3$, is 15 mJy while all other models have a mean quiescent flux of less than 1 mJy. Models C and D both show flaring of approximately the right magnitude (an average of about 25 mJy during the flare and less than 1 mJy during the quiescent period) and duration (approximately 1–2 h).

Fig. 7 shows a histogram of F_ν for all models compared to the observational constraints listed in Section 1. The thermal model (A) never produces the high fluxes seen during flares while the constant non-thermal fraction model (B) never produces the observed variability. The non-thermal injection models fit the observed flux distribution better, with model C producing a slope that is closer to the observations than model D. None of the four models match the low flux (<3.5 Jy) portion of the distribution, though this portion is subject to large observational uncertainties (Dodds-Eden et al. 2011).

Fig. 8 shows a set of NIR images (for models A and D) during a flare, at $t = 550\ GM_{\rm BH}/c^3$. Flaring images are highly variable, but they all show substantial emission from the mid–plane close to the innermost stable circular orbit (ISCO); this is true for all models that show flares. A similar set of NIR images is shown in Fig. 9. This set of images is from a representative quiescent state ($t = 1700\ GM_{\rm BH}/c^3$); all non-thermal models show similar behaviour, with nearly all of the emission coming from the mid-plane around or within the ISCO.

Fig. 10 shows the wander of the NIR image centroid over the course of the simulation. The background image is the same as the central portion of the right image in Fig. 8. The image centroids, calculated for every point with more a flux density of more than 5-m Jyon the NIR light curve of model D in Fig. 6, are represented by the white dots. There is no significant trend in image centroid location with flux for 2.2 -μm emission and all but four of the centroids (about 0.3 per cent) lie within 10 μas of the mean. The centroid has a root-mean-square deviation of 4.9 μas from its average position. Models B and C have no centroid deviations of more than 5 μas.

Thus far, we have assumed that the disc is viewed nearly edge on (with an inclination angle of 84°) while GRAVITY finds an inclination angle of 160° ± 10° (Gravity Collaboration 2018). Fig. 11 shows that the NIR light curve and image wander are not strongly dependent on inclination angle (keeping all other parameters constant). The root-mean-square centroid deviation is found by first calculating the mean location of the centroid from each frame of the light curve and then finding the root-mean-square separation between that mean location and each frame's centroid. This rms separation is always less than the minimum detectable separation for GRAVITY (10 μas). Further, all inclination angles show similar NIR variability. This result may change in non-axisymmetric models.

4.3 Spectral energy densities

The SEDs for all four models are shown in Fig. 12, with the left-hand panel showing a model flare and the left showing the modelled quiescent state. In both panels, the computed SEDs are compared to the observed mm luminosity and the NIR flaring/non-flaring luminosity and NIR spectral slope listed in Section 1. The pure thermal model produces negative spectral slopes while the non-thermal models come within about 10 per cent of 0.4, as was expected from our choice of κ.

4.4 J^2 distribution

Fig. 13 shows the spatial distribution of J^2 during a flare and during quiescence ($t = 550\ GM_{\rm BH}/c^3$ and $t = 1700\ GM_{\rm BH}/c^3$, respectively). During the flare, the total current is larger (J^2 integrated over the domain is 10 times what it is during quiescence) and there are multiple current sheets near (but not in) the mid-plane within the ISCO radius. During quiescence, the current tends to be further out and less concentrated. Fig. 14 shows how current density varies with radius for both flaring and quiescent states. Due to the grid refinement, current densities are larger in smaller zones (near the mid-plane and at low radius).

5 DISCUSSION

All models agree with 230- GHz observations of Sgr A*'s size and average flux by construction. The variability for all four models is close to the observed variability. The addition of non-thermal electrons in models B, C, and D does not change the SED at $\lambda \approx 1.3$ mm.

Three models (B, C, and D) were able to replicate the 2.2-μm flux during a flare while the purely thermal model, predictably, failed to do so. The models that inject non-thermal electrons in reconnecting current sheets were also able to reproduce the observed variability with one large flaring event of about an hour (∼10 orbital periods at the ISCO) in duration and with a power-law tail at large flux. The power-law slope for model C (−2.5) is close to the observed slope (−2.7) while the slope for model D (−1.5) is still encouraging

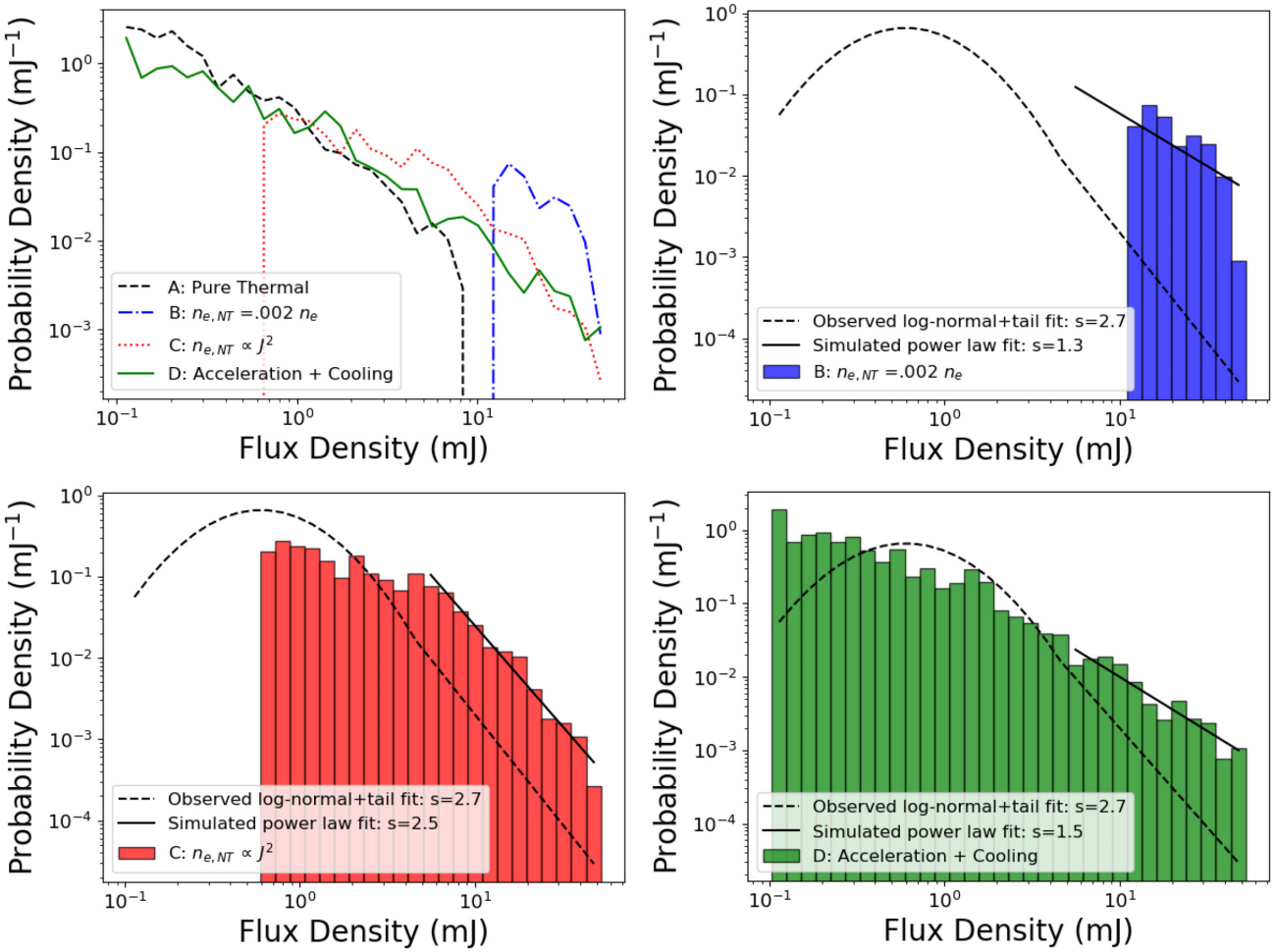

Figure 7. *Top left:* Line plots of the flux frequency histograms for models A–D. *Top right:* Histogram for model B only along with the lognormal + tail fit (dashed line) reported in Dodds–Eden et al. (2011) and a power-law fit (solid line) to the simulated tail section (all fluxes greater than 5 mJy). *Bottom left:* Histogram for model C with the same fit lines. *Bottom right:* Histogram for model D with the same fit lines.

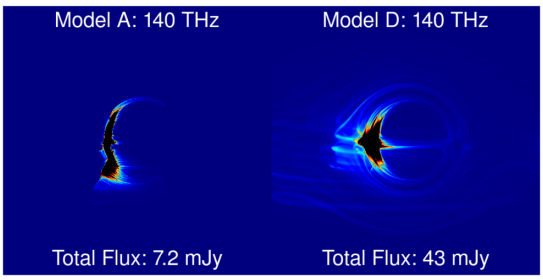

Figure 8. Images at 2.2 μm during a flare ($t = 550\ GM_{\rm BH}/c^3$). *Top*: Model A. *Bottom*: Model D. Each image has a separate, linear colour map.

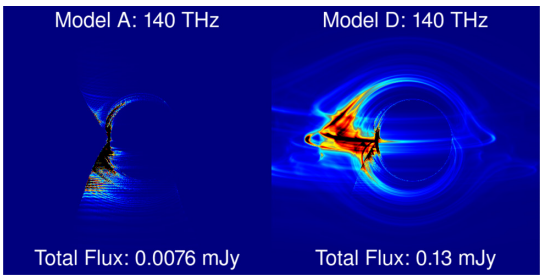

Figure 9. Images at 2.2 μm from $t = 1700\ GM_{\rm BH}/c^3$(during a quiescent period). *Top*: Model A. *Bottom*: Model D. Each image has a separate, linear colour map.

for this preliminary, axisymmetric model. Of course, we are really looking only at the shape of a single flare; we expect a more definitive probability distribution function of flux densities from future, 3D models that are capable of producing multiple flares.

The fraction of electrons in the non-thermal component can be estimated by assuming that the spectral index of $\alpha = 0.4$ is valid for the non-thermal electrons from 230 GHz to 140 THz and comparing the mean mm flux density to the flaring NIR flux density. In this approximation, a small fraction of non-thermal electrons can account for the non-thermal NIR emission. In model B, the non-thermal fraction is < 1 per cent and by construction is uniform across the model; in models C and D, the non-thermal fraction is of order 10 per cent in regions of high current density and much smaller elsewhere in the model.

The centroid location of the 2.2-μm images shows no correlation with the 2.2-μm flux. Further, the centroid wander, which is confined to a ∼10 μas region, is too small to be seen by GRAVITY, which has 10 μas precision. If this model is correct, then it is in conflict with the GRAVITY results, which show centroid motion of around

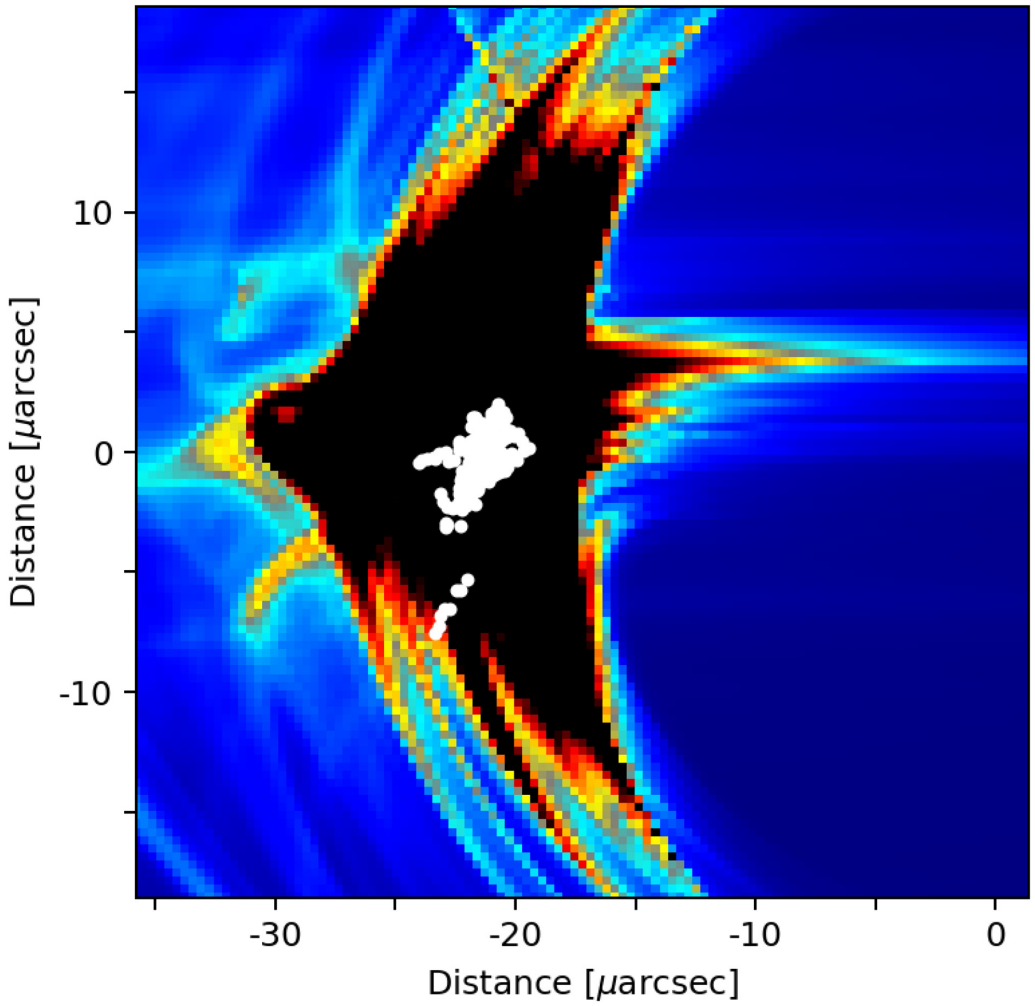

Figure 10. The track of the centroid of 2.2- μm emission overplotted on a background of the central portion of the flaring image in Fig. 8. The white dots correspond to centroid locations when the total flux density was greater than 5 mJy.

150 μas (Gravity Collaboration 2018). It is possible, however, that a full 3D simulation, perhaps a highly variable model with large magnetic flux (magnetically arrested disc, MAD, model), with a face-on orientation, will show greater centroid variability.

5.1 Comparison to earlier work

Sgr A* shows variability in the NIR that results in flares more than an order of magnitude brighter than the non-flaring state (see Section 1). Several authors have found flares using a variety of both thermal and non-thermal models, though none of them result in both sufficient flare amplitude and the correct NIR spectral index.

Dexter & Fragile (2013) consider an accretion disc that is not aligned with the spin axis of the black hole (a 'tilted' disc). This creates standing shocks that heat electrons in the inner portion of the disc. Radiation from these hotspots is gravitationally lensed, leading to NIR flares with close to the observed maximum flux. The NIR spectral slope depends sharply on the black hole spin and the inclination of the disc. Also, the image centroid shifts by 30–50 μas independently of the NIR flux.

Chan et al. (2015) propose that infrared flares are caused by gravitational lensing of magnetically dominated regions. Using GRMHD simulations, a difference is apparent between low-magnetic flux models (standard and normal evolution, SANE, models) and high-magnetic flux models (MAD models; Narayan et al. 2012). The SANE models produce a lognormal distribution of fluxes at 2.2 μm while the MAD models produce a flat distribution at large fluxes. These models all produce SEDs with a negative spectral index in the NIR region.

In Chael et al. (2018), two-temperature 3D GRMHD SANE simulations are evolved for $1.5 \times 10^4\, GM_{\rm BH}/c^3$. Two models were used to partition dissipation between electrons and ions. The first, based on Howes (2010), models dissipation at the bottom of an Alfvénic cascade, while the second is based on reconnection models from Rowan, Sironi & Narayan (2017). Flares were observed, but the flare/quiescent flux ratio is at least half an order of magnitude lower than observed. Further, the spectral slope is always too negative in the NIR.

Previous work has also attempted to explain the variability of Sgr A* by introducing a non-thermal electron distribution function. Yuan, Quataert & Narayan (2003) replaces a constant fraction (a few per cent by energy) of the electrons in a radiatively inefficient accretion flow model with a power-law distribution function. By manipulating the power-law index, it is possible to produce an increase in the infrared emission. Chan et al. (2009) use a distribution function that is thermal at low γ and a broken power law at high γ.

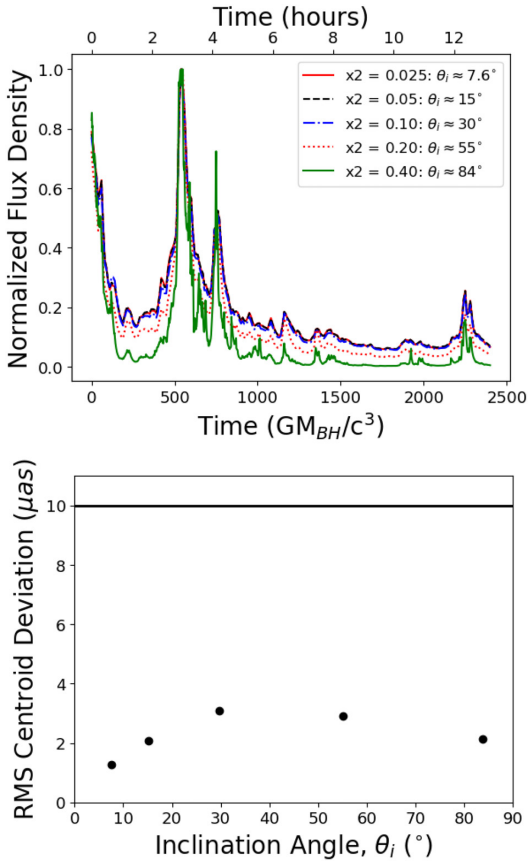

Figure 11. *Top:* Normalized light curves for various inclination angles (all other parameters constant). *Bottom:* rms centroid deviation at various inclination angles (points) compared to GRAVITY astrometric precision (solid line).

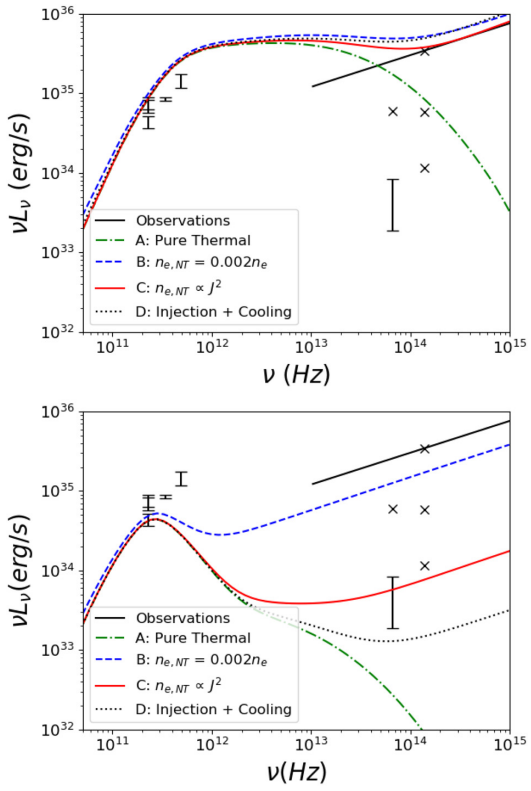

Figure 12. Model SEDs compared with observations. *Top:* models during a flare (at $t = 550\ GM_{\rm BH}/c^3$). *Bottom:* models in a quiescent state (at $t = 1700\ GM_{\rm BH}/c^3$). Observational data, mm luminosity as well as the flaring/non-flaring luminosity and spectral slope, are from Dodds-Eden et al. (2011), Fish et al. (2011), García-Marín et al. (2011), Witzel et al. (2012), Bower et al. (2013), Hora et al. (2014), Bower et al. (2015), and Liu et al. (2016).

By introducing a Gaussian density perturbation, perhaps produced by clumpy infall on to the disc, they were able to produce a flare.

In Dodds-Eden et al. (2010), heating is included via an explicit resistivity in axisymmetric pseudo-Newtonian MHD models, and these in turn motivate parameters for a one-zone NIR emission model. The one-zone models include synchrotron cooling, which leads to a cooling break, and a change in the spectral index (by $\Delta\alpha = 0.5$) between the X-ray and NIR. The resulting NIR light curves exhibit flares lasting for somewhat longer than an hour (depending on the parameters used) and flares in the X-ray that are shorter than an hour. The difference in flare duration in NIR and X-ray can be explained by electrons that produce X-rays cooling faster than electrons that produce NIR radiation.

Kusunose & Takahara (2011) posited that a pocket of plasma, escaping from near the black hole, contains a population of power-law electrons. This produced a flare with approximately the correct spectral slope, though the slope varied during the flare, but the model did not produce any quiescent NIR emission. Ball et al. (2016) present a GRMHD model in which non-thermal electrons are accelerated in regions in which the plasma β falls below a critical value. The non-thermal electrons are cooled by synchrotron radiation. This produces variability in both the NIR (with flares $\sim$2 orders of magnitude above the quiescent flux) and X-ray (with flares $\sim$1 order of magnitude above the quiescent flux) regions. Although observations show $\nu L_\nu \propto \nu^\alpha$ with $\alpha > 0$, the model shows $\alpha < 0$.

Chael, Narayan & Saḍowski (2017) present a sophisticated 2D general relativistic radiative magnetohydrodynamic (GRRMHD) simulation including non-thermal electrons. The electron distribution function was evolved over time and included advection, injection (into a power-law component) based on the viscous heating, and cooling due to adiabatic effects, synchrotron radiation, inverse Compton scattering, bremsstrahlung, and Coulomb coupling. The effect was to increase the high-frequency (NIR and above) emission from large radii. Due to the lack of rapid fluctuations at large radii, this leads to very little NIR variability.

Davelaar et al. (2018) describe a model that includes electrons in a κ distribution in the jet sheath, while the disc was assumed to be completely thermal. With 1 per cent of the electrons, by energy, in the κ distribution, the NIR spectral slope and quiescent flux were matched to observations while flares were matched with 5 per cent to 10 per cent of the electrons in the κ distribution. This work was aimed at matching the observed SED and did not generate light curves.

6 CONCLUSION

EHT will soon provide high spatial resolution mm observations of Sgr A*, and GRAVITY has produced 10 μas precision astrometry of Sgr A*in the NIR in a flaring state. However, the infrared properties of Sgr A* have been difficult to model. The spectral slope in the NIR region suggests the presence of a non-thermal electron population

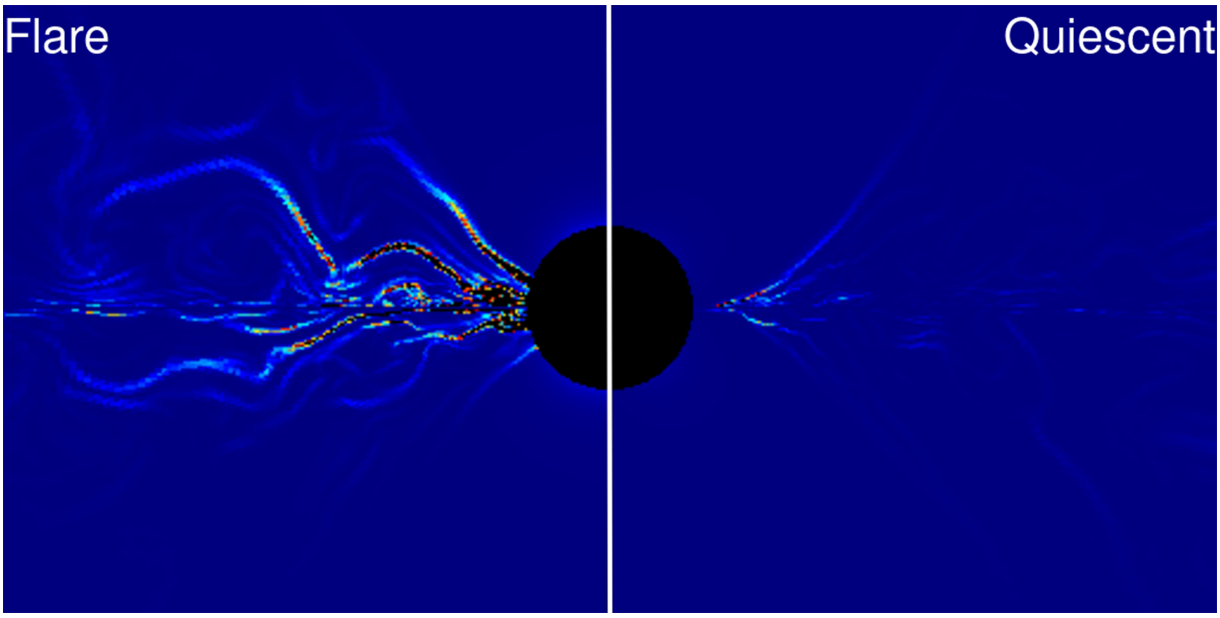

Figure 13. Maps of J^2 out to $r = 10\,GM_{\rm BH}/c^2$ and within $5\,GM_{\rm BH}/c^2$ of the mid-plane. *Left*: During a flare ($t = 550\,GM_{\rm BH}/c^3$). *Right*: During a quiescent period ($t = 1700\,GM_{\rm BH}/c^3$). The flare and quiescent colour scales are different; the total (squared) current integrated over the domain is 10 times larger in the flare than during quiescence.

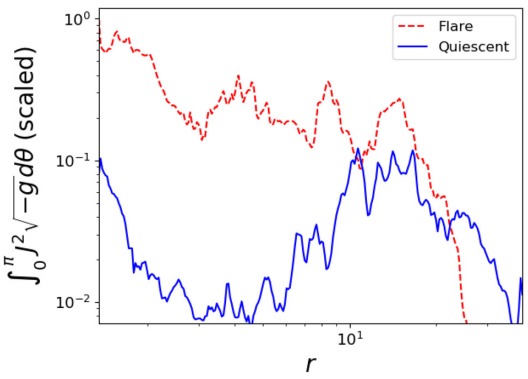

Figure 14. Distribution of current density integrated over polar angle versus radius. In the flaring state, the currents are highest at low radius while the average radius for current in the quiescent state is much further out. Currents for the quiescent state never get much over one-tenth of the currents in the inner region for the flaring state.

and the presence of flares more than an order of magnitude brighter than the quiescent state indicates intense, rapid variability. Previous models have been unable to successfully reproduce all of these features. In this paper, we have produced synthetic NIR light curves based on GRMHD models that incorporate a model for accelerating electrons from a thermal distribution into a power-law tail.

A control model, which contains only thermal electrons, produces no significant NIR emission. A simple non-thermal model that places a constant fraction of the electrons into a non-thermal (κ distribution) component is able to produce the correct spectral slope and flaring flux density but not the variability. The next simplest model is based on the idea that electrons are accelerated due to resistive dissipation in reconnecting current sheets and, therefore, sets the fraction of electrons in the non-thermal distribution proportional to J^2, where J is the 3-current density measured in the plasma frame. This model matches the spectral slope and flaring emission but also matches the flux density distribution fairly well. A final model fares similarly in matching observations but is both better motivated physically and more computationally expensive. It advects the non-thermal electrons with the fluid, accelerates electrons into the non-thermal component at a rate proportional to J^2, and allows them to cool using a constant cooling time model. Because these last two models agree with each other relatively well, future work will focus on the simpler one. No model shows substantial NIR centroid wander or any correlation between the NIR flux density and image centroid.

These models are the first to accurately produce the observed Sgr A* mm mean flux, mm image size NIR spectral slope, flare duration, and flux distribution at the same time. Future work will adapt these models to 3D and will include Compton scattering in order to examine X-ray flares.

ACKNOWLEDGEMENTS

This work was supported by National Science Foundation grants AST 17-16327 and PIRE 17-4374. We are grateful to George Wong for his thoughtful comments.

REFERENCES

Abuter R. et al., 2019, A&A, 625, L10,
Baganoff F. K. et al., 2001, Nature, 413, 45
Balick B., Brown R. L., 1974, ApJ, 194, 265
Ball D., Özel F., Psaltis D., Chan C.-k., 2016, ApJ, 826, 77
Biskamp D., 1996, Ap&SS, 242, 165
Boehle A. et al., 2016, ApJ, 830, 17
Bower G. C., Falcke H., Wright M. C., Backer D. C., 2005, ApJ, 618, L29
Bower G. C., Plambeck D., Marrone D., 2013, Astron. Telegram, 5018
Bower G. C. et al., 2015, ApJ, 802, 69
Cerutti B., Werner G. R., Uzdensky D. A., Begelman M. C., 2012, ApJ, 754, L33
Cerutti B., Werner G. R., Uzdensky D. A., Begelman M. C., 2013, ApJ, 770, 147

Cerutti B., Werner G. R., Uzdensky D. A., Begelman M. C., 2014, ApJ, 782, 104
Chael A. A., Narayan R., Sądowski A., 2017, MNRAS, 470, 2367
Chael A., Rowan M., Narayan R., Johnson M., Sironi L., 2018, MNRAS, 478, 5209
Chan C.-k., Liu S., Fryer C. L., Psaltis D., Özel F., Rockefeller G., Melia F., 2009, ApJ, 701, 521
Chan C.-k., Psaltis D., Özel F., Medeiros L., Marrone D., Sądowski A., Narayan R., 2015, ApJ, 812, 103
Chasapis A. et al., 2018, ApJ, 862, 32
Cohen R. H., Kulsrud R. M., 1974, Phys. Fluids, 17, 2215
Davelaar J., Mościbrodzka M., Bronzwaer T., Falcke H., 2018, A&A, 612, A34
Dexter J., 2016, MNRAS, 462, 115
Dexter J., Fragile P. C., 2013, MNRAS, 432, 2252
Do T., Ghez A. M., Morris M. R., Yelda S., Meyer L., Lu J. R., Hornstein S. D., Matthews K., 2009, ApJ, 691, 1021
Dodds-Eden K. et al., 2009, ApJ, 698, 676
Dodds-Eden K., Sharma P., Quataert E., Genzel R., Gillessen S., Eisenhauer F., Porquet D., 2010, ApJ, 725, 450
Dodds-Eden K. et al., 2011, ApJ, 728, 37
Doeleman S. S. et al., 2008, Nature, 455, 78
Eisenhauer F. et al., 2008, in Proc. SPIE Conf. Ser. Vol. 7013, Optical and Infrared Interferometry. SPIE, Bellingham,p. 70132A
Event Horizon Telescope Collaboration, 2019a, ApJ, 875, L1
Event Horizon Telescope Collaboration, 2019b, ApJ, 875, L2
Event Horizon Telescope Collaboration, 2019c, ApJ, 875, L3
Event Horizon Telescope Collaboration, 2019d, ApJ, 875, L4
Event Horizon Telescope Collaboration, 2019e, ApJ, 875, L5
Event Horizon Telescope Collaboration, 2019f, ApJ, 875, L6
Falcke H., Goss W. M., Matsuo H., Teuben P., Zhao J.-H., Zylka R., 1998, ApJ, 499, 731
Falcke H., Markoff S., Bower G. C., Gammie C. F., Mościbrodzka M., Maitra D., 2011, in Romero G. E., Sunyaev R. A., Belloni T., eds, Proc. IAU Symp. 275, Jets at All Scales. Kluwer, Dordrecht, p. 68 preprint (arXiv:1010.5239)
Fish V. L. et al., 2011, ApJ, 727, L36
Fishbone L. G., Moncrief V., 1976, ApJ, 207, 962
Gammie C. F., McKinney J. C., Tóth G., 2003, ApJ, 589, 444
García-Marín M. et al., 2011, ApJ, 738, 158
Gary S. P., Zhao Y., Hughes R. S., Wang J., Parashar T. N., 2018, ApJ, 859, 110
Genzel R., Schödel R., Ott T., Eckart A., Alexander T., Lacombe F., Rouan D., Aschenbach B., 2003, Nature, 425, 934
Genzel R., Eisenhauer F., Gillessen S., 2010, Rev. Mod. Phys., 82, 3121
Ghez A. M. et al., 2005, ApJ, 635, 1087
Ghez A. M. et al., 2008, ApJ, 689, 1044
Gillessen S. et al., 2006, ApJ, 640, L163
Gillessen S., Eisenhauer F., Trippe S., Alexander T., Genzel R., Martins F., Ott T., 2009, ApJ, 692, 1075
Gravity Collaboration, 2018, A&A, 618, L10
Guo X., Sironi L., Narayan R., 2018, ApJ, 858, 95
Haubois X. et al., 2012, A&A, 540, A41
Hora J. L. et al., 2014, ApJ, 793, 120
Hornstein S. D., Matthews K., Ghez A. M., Lu J. R., Morris M., Becklin E. E., Rafelski M., Baganoff F. K., 2007, ApJ, 667, 900
Howes G. G., 2010, MNRAS, 409, L104
Kawazura Y., Barnes M., Schekochihin A. A., 2018, Proc. Natl. Acad. Sci., 116, 771
Kunz M. W., Stone J. M., Quataert E., 2016, Phys. Rev. Lett., 117, 235101
Kusunose M., Takahara F., 2011, ApJ, 726, 54
Liu W., Li H., Yin L., Albright B. J., Bowers K. J., Liang E. P., 2011, Phys. Plasmas, 18, 052105
Liu H. B. et al., 2016, A&A, 593, A44
Loureiro N. F., Boldyrev S., 2017, ApJ, 850, 182
Loureiro N. F., Schekochihin A. A., Cowley S. C., 2007, Phys. Plasmas, 14, 100703
Makwana K., Li H., Guo F., Li X., 2017, J. Phys. Conf. Ser., 837, 012004
Marrone D. P., Moran J. M., Zhao J.-H., Rao R., 2006, in Schödel R., Bower G. C., Muno M. P., Nayakshin S., Ott T., eds, J. Phys. Conf. Ser., 54, 354
Marrone D. P. et al., 2008, ApJ, 682, 373
McKinney J. C., Gammie C. F., 2004, ApJ, 611, 977
Miesch M. et al., 2015, Space Sci. Rev., 194, 97
Misner C. W., Thorne K. S., Wheeler J. A., 1973, Gravitation. W. H. Freeman, https://www.xarg.org/ref/a/0716703440/
Mościbrodzka M., Gammie C. F., 2018, MNRAS, 475, 43
Mościbrodzka M., Gammie C. F., Dolence J. C., Shiokawa H., Leung P. K., 2009, ApJ, 706, 497
Narayan R., SÄ dowski A., Penna R. F., Kulkarni A. K., 2012, MNRAS, 426, 3241
Noble S. C., Leung P. K., Gammie C. F., Book L. G., 2007, Class. Quantum Gravity, 24, S259
Özel F., Psaltis D., Narayan R., 2000, ApJ, 541, 234
Padmanabhan P., 2000, Theoretical astrophysics. Vol.1: Astrophysical processes. Cambridge Univ. Press, Cambridge
Pandya A., Zhang Z., Chandra M., Gammie C. F., 2016, ApJ, 822, 34
Pierrard V., Lazar M., 2010, Sol. Phys., 267, 153
Ponti G. et al., 2015, MNRAS, 454, 1525
Qin G., Kong F.-J., Zhang L.-H., 2018, ApJ, 860, 3
Ricarte A., Dexter J., 2015, MNRAS, 446, 1973
Riquelme M. A., Quataert E., Sharma P., Spitkovsky A., 2012, ApJ, 755, 50
Rowan M. E., Sironi L., Narayan R., 2017, ApJ, 850, 29
Shiokawa H., Dolence J. C., Gammie C. F., Noble S. C., 2012, ApJ, 744, 187
Sironi L., Spitkovsky A., 2014, ApJ, 783, L21
Siversky T. V., Zharkova V. V., 2009, Journal of Plasma Physics, 75, 619
Tóth G., 2000, Journal of Computational Physics, 161, 605
van Marle A. J., Casse F., Marcowith A., 2018, MNRAS, 473, 3394
Vasyliunas V. M., 1968, J. Geophys. Res., 73, 2839
Verniero J. L., Howes G. G., Klein K. G., 2018, J. Plasma Phys., 84, 905840103
Witzel G. et al., 2012, ApJS, 203, 18
Witzel G. et al., 2018, ApJ, 863, 15
Yuan F., Narayan R., 2014, ARA&A, 52, 529
Yuan F., Quataert E., Narayan R., 2003, ApJ, 598, 301

APPENDIX A: DISSIPATION IN RELATIVISTIC MHD

Here, we prove that heating rate per unit volume due to resistive dissipation (the dissipation function) is J^2/σ if we adopt the simplest covariant model for Ohm's law.

Maxwell's equations are

$$j^\mu = F^{\mu\nu}{}_{;\nu}. \tag{A1}$$

Project this into the space normal to the plasma four-velocity u^μ using the projection tensor

$$h^\mu_\nu \equiv g^\mu_\nu + u^\mu u_\nu \tag{A2}$$

and define the projected current

$$J^\mu \equiv h^\mu_\nu j^\nu. \tag{A3}$$

If we then write a simple model for Ohm's law as

$$J^\mu = \sigma F^\mu{}_\nu u^\nu \tag{A4}$$

where σ is the conductivity, it is easy to show that this reduces to the familiar form of Ohm's law for a scalar conductivity.

To evaluate the dissipation function, observe that since

$$T^{\mu\nu}{}_{;\nu} = 0, \qquad (\rho u^\mu)_{;\mu} = 0 \tag{A5}$$

then

$$u_\mu T^{\mu\nu}{}_{;\nu} + (\rho u^\mu)_{;\mu} = 0. \tag{A6}$$

For an ideal fluid stress-energy tensor, this implies

$$u^{\nu}u_{;\nu} + (u + p)u^{\nu}{}_{;\nu} = 0 \tag{A7}$$

where u is internal energy and p is pressure. This is just the internal energy equation as derived from the first law assuming the dissipation function $\rho T \mathrm{d}s/\mathrm{d}\tau = \rho T u^{\mu} s_{;\mu} = 0$. Here, the scalars $s \equiv$ entropy and $T \equiv$ temperature.

Now consider a magnetized fluid and break the stress-energy tensor into an ideal fluid and electromagnetic piece, $T^{\mu\nu} = T^{\mu\nu}_{\mathrm{FL}} + T^{\mu\nu}_{\mathrm{EM}}$. Then

$$u_{\mu}T^{\mu\nu}_{;\nu} + (\rho u^{\mu})_{;\mu} = 0 = -\rho T u^{\mu} s_{;\mu} - u^{\mu}T^{\mu\nu}_{\mathrm{EM};\nu}. \tag{A8}$$

From MTW, Misner et al. (1973), exercise 22.10 (which uses a symmetry argument and Maxwell's equations)

$$T^{\beta}_{\mathrm{EM}\alpha;\beta} = -F_{\alpha\mu}j^{\mu}. \tag{A9}$$

Combining,

$$\rho T u^{\mu} s_{;\mu} = -u^{\alpha}\left(-F_{\alpha\mu}j^{\mu}\right). \tag{A10}$$

Then Ohm's law implies

$$\rho T u^{\mu} s_{;\mu} = \frac{1}{\sigma}J^{\mu}j_{\mu} = \frac{J^2}{\sigma}. \tag{A11}$$

This is positive definite because J^{μ} is spacelike by construction and, therefore, the second law is satisfied.

APPENDIX B: PARAMETER IMPORTANCE

Model D, described in the text, depends on the parameters κ (the slope of the power-law tail of the electron distribution function) and τ (the cooling time for the non-thermal electrons). How do the light curves depend on these parameters?

B1 Dependence on τ_{cool}

If the non-thermal electrons are in equilibrium, equation (3) can be set to zero. Further, if $n_{\mathrm{e,\,NT}}/n_{e,\,\mathrm{total}}$ is small (which is equivalent to small $\eta\tau_{\mathrm{cool}}$), then the non-thermal electron density (which is proportional to the NIR emission) is proportional to the product $\eta\tau_{\mathrm{cool}}$. This is illustrated by Fig. B1, which shows the average and peak flux for light curves of several variants of model D. This shows that it is the product of η and τ_{cool} that determines the flare amplitudes.

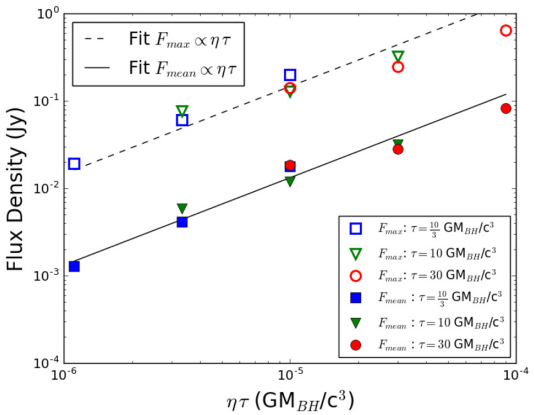

Figure B1. Mean and peak flux as a function of $\eta\tau_{\mathrm{cool}}$ for nine light curves based on model D with various values of η and τ_{cool}.

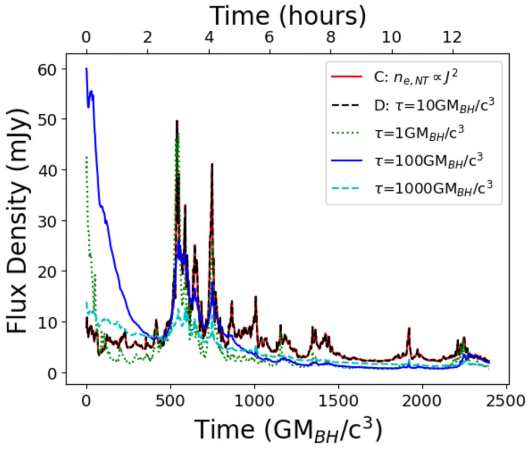

Figure B2. NIR light curves for variations of model D with differing τ_{cool} but constant $\eta\tau_{\mathrm{cool}}$. Long τ_{cool} flares show a larger FWHM as model D while short cooling time flares are almost identical as the FWHM of these flares are dominated by the duration of the reconnection event, not the electron cooling time-scale.

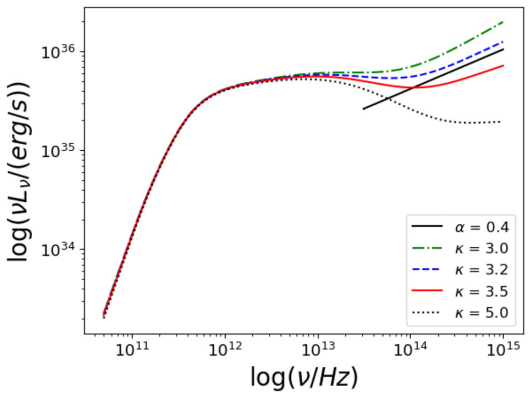

Figure B3. SEDs from variations of model D during a flare ($t = 500\ GM_{\mathrm{BH}}/c^3$). The expected value of κ reproduces the observed slope in the NIR region.

Fig. B2 shows the effect that changing η and τ_{cool} (with $\eta\tau_{\mathrm{cool}}$ constant) has on the light curve. For large enough cooling times, increasing τ_{cool} increases the FWHM of the flare. As τ_{cool} becomes shorter, however, this ceases to be the case as the duration of the reconnection event ensures that electrons are continuously accelerated even as they cool. This justifies the use of model C, which is the short cooling time limit of model D. Evidently, η affects the amplitude of the flare while τ_{cool} affects both the amplitude and the duration.

B2 Dependence on κ

Equation (2) relates κ to the spectral slope in the NIR. However, there is some degree of tension between the observed spectral slope and the κ found from PIC simulations. Fig. B3 shows the SEDs during a flare for variations of model D with several values of κ. This plot shows that equation (2) is valid during the flare and that $\kappa = 3.2$ provides the best match to observations.

This paper has been typeset from a TEX/LATEX file prepared by the author.